University of Bath

Alternative formats
If you require this document in an alternative format, please contact:
openaccess@bath.ac.uk

Continuous rotary membrane emulsification for the production of sustainable Pickering emulsions

Ekanem E. Ekanem, [a,b] * *Amy Wilson,* [c, d] *Janet L. Scott,* [c, d] *Karen Edler,* [c, d] *and Davide Mattia,* [a,b,d] *

[a] Department of Chemical Engineering, University of Bath, Claverton Down, Bath, BA2 7AY, United Kingdom.

[b] Centre for Advanced Separations Engineering, University of Bath, Claverton Down, Bath, BA2 7AY, United Kingdom.

[c] Department of Chemistry, University of Bath, Claverton Down, Bath, BA2 7AY, United Kingdom.

[d] Centre for Sustainable and Circular Technologies, University of Bath, Claverton Down, Bath, BA2 7AY, United Kingdom.

* **Corresponding Author**s:

Email: e.e.ekanem@bath.ac.uk (E.E.Ekanem), d.mattia@bath.ac.uk (D.Mattia)

Abstract:

A continuous rotary membrane emulsification (cRME) system, allowing the decoupling of droplet generation from continuous phase (CP) flowrate, is presented here for the first time. The decoupling results in higher productivity and greater control compared to traditional crossflow and rotational membrane emulsification processes. A design of experiment (DoE) investigated the influence on droplet formation of CP flow, membrane rotational speed and emulsion composition, using a Pickering emulsion consisting of 1 wt% keratin solution and varying concentrations of oxidised cellulose nanofibrils. Experiments showed that CP flowrate had a negligible effect on droplet diameters in a wide range (between 78 and 241 μm), with uniformity index as low as 0.14 for optimal membrane rotational speeds and different oxidised cellulose nanofibrils (OCNF) concentration.

cRME has the potential to overcome low emulsion concentration limitations of continuous membrane emulsification systems, paving the way to significantly increase the productivity and application in personal care, food and drugs industries.

Keywords: Rotary membrane emulsification, Monodisperse emulsion, Pickering emulsions, 3-D printing, Stainless steel membrane. Sustainability.

2

1. Introduction

Membrane emulsification (ME) is a technology to generate monodisperse droplets in which the disperse phase (DP) is extruded, dropwise, into the continuous phase (CP) through a microporous membrane [1]. Droplet detachment in the continuous phase is driven by forces associated with the DP flux and interfacial tension (IFT), and facilitated by shear force at the membrane surface imparted by the CP. Most ME rigs are operated batchwise [2-5] or semi-continuously [6-9]. Compared with traditional top-down emulsification methods (such as high-pressure homogenisation or rotor stator systems), membrane emulsification's bottom-up approach allows for lower energy usage, lower shear rates and more precise control over droplet size and uniformity, leading to a wide scope of applications in food, cosmetics and pharmaceuticals [10].

Abbreviations: ANOVA, Analysis of Variation; CCF, Central Composite Face design; CP, continuous phase; Dd_{DOE}, experimental diameter from developed DOE model; Dd_K, theoretical droplet diameter magnitudes estimated from a force balance model. DoE, Design of Experiment; IFT, interfacial tension; ME, Membrane emulsification; MLR, Multiple Linear Regression; n, rotational speed; OCNF, oxidised cellulose nanofibrils; Q^2, prediction precision; RME, rotary membrane emulsification; R^2, model fit ; Ta, Taylor number; XME, cross-flow membrane emulsification; x_w, OCNF concentration; Re, Reynolds number; R_1, radius of membrane tube; R_2, radius of stationary cylinder; Q_{CP}, continuous phase flowrate; ρ, density; η, viscosity of continuous phase; ω, angular velocity.

A limitation of ME, however, is its characteristic low concentration output. Cross-flow membrane emulsification (XME), in which droplets are generated when the DP permeates through a membrane into a cross flowing CP, has been demonstrated at pilot plant scale as a batch and semi-continuous automated process [11]. Although XME can operate continuously, the high CP flow rates required relative to the DP flux result in emulsions with low DP concentration, giving significantly lower outputs than industrial homogenisers [12]. Nevertheless, the emulsion can be recirculated through the system to increase the DP concentration to an acceptable level. This reverts the process to a semi-continuous one and can negatively affect the emulsion quality due to droplet coalescence in process equipment such as pumps and valves [10]. To meet shear and concentration requirements for monodisperse droplet generation, potential mitigating solutions include introducing an axial oscillatory pulsation of the CP [6, 7], or the oscillatory pulsation of the membrane (axially [13] or azimuthally [14]) to accumulate more droplets. Regardless, these oscillatory solutions have higher energy demands compared to the simple XME systems [15]. A recent alternative has involved inserting a rod inside the lumen of a tubular membrane to limit the cross flowing CP to a narrow annular channel, which also increases droplet shear [16]. While this approach can produce emulsions at industrial scale with higher emulsion concentrations and solves the high shear requirement, the sensitivity to CP flow perturbations is increased, reducing droplet size control, and different inner rod diameters are needed to obtain targeted shear ranges.

In rotary membrane emulsification (RME), the DP is extruded from a rotating tubular membrane into the surrounding CP, and the membrane wall shear generated on the surface of the membrane facilitates droplet detachment [17, 18]. The DP is allowed to concentrate to a

desired level before terminating the process, which eliminates the need to recirculate the emulsion, reducing energy consumption, running costs, and risk of damage to droplets [4]. However, this is a semi-continuous process, making scale up challenging. Combining a continuous flow with rotating membranes to generate emulsions showed that membrane rotational speed, the annular gap width between rotating membrane and stationary cylinder, and DP volume fraction were the main factors affecting the size and uniformity of generated droplets [19]. This study, however, did not investigate the potential to decouple droplet generation from CP flow rate, a key requirement to combine the advantages of XME and RME.

In this work a novel flow cell was designed and 3-D printed to decouple CP flow rate from shear generation and enable controlled vortex generation, thereby transforming the RME into a continuous process. To demonstrate the compatibility of this novel continuous RME (cRME) system with contemporary sustainable emulsion generation, sustainable biomaterials such as soluble keratin and oxidised cellulose nanofibrils (OCNF) were used as a sunflower oil (DP) emulsifier and viscosity modifier, respectively. Biopolymers are increasingly being investigated as emulsion stabilisers, for their renewable, biodegradable and often surface-active properties. Proteins and polysaccharides are commonly used in such applications, for example, recent works describe the use of cellulose nanofibrils [20], zein nanoparticles [21] and pea protein microgels [22] as Pickering stabilizers for emulsions. Keratin, in particular, is a surface-active protein [23] solubilised from waste wool or feathers [24], making it a renewable and inexpensive source of emulsifier. OCNF are produced from cellulose, the most abundant biopolymer on the planet, with minimal chemical processing, presenting an inexpensive and renewable plant-derived aqueous rheology modifier [25].

2. Materials and Methods

2.1 Materials

Sunflower oil supplied by Tesco was used as the dispersed phase. Clean Sheep wool obtained from Wingham Wool Work, UK, was used as a source of keratin. A TEMPO-oxidized cellulose nanofibril (OCNF) dispersion was a kind gift from CRODA UK and used to increase the viscosity of the continuous phase.

2.2 Continuous Phase Preparation

A stock keratin solution was prepared by sulfitolytic extraction from clean sheep wool based on previously reported methods of keratin extraction [26]: To a pH-neutralized solution of 8 M urea, 0.5 M sodium metabisulfite, 0.2 M tris base and 0.2 M SDS, 40 g wool were added. The solution was then heated for 5 h at 65 °C while stirring to extract keratin. Following extraction, residual wool solids were removed by sieving (100 um mesh) before dialysis against deionized water was carried out on the keratin solution for 3 days with daily replacement of water. The resulting solution contained 2.4 wt% keratin following analysis using a loss on drying method.

A stock OCNF dispersion (degree of oxidation ~25%, measured by conductimetric titration) was obtained by dilution and purification of a concentrated paste (~8 wt%), using a published method to remove residual salts and preservatives and ensure an adequate, stable dispersion of OCNF [27, 28]. Briefly, the paste was diluted in deionized water, adjusted to pH 3, dialyzed against deionized water, homogenized, adjusted to pH 7, dialyzed again and then dispersed using an ultrasonic probe until transparent. The resulting dispersion contained 2 wt% OCNF. The concentration (wt%) of ~10ml of each stock was determined by lyophilization, calculated using the initial mass of the sample and the mass of the solids remaining following

lyophilization. An average of three measurements were taken. The stock keratin solution and OCNF dispersion were mixed and diluted to produce continuous phase preparations of 1 wt% keratin concentration and varying OCNF concentration (0.5, 0.75 or 1 wt%).

2.3 Viscosity measurement

The rheology of the disperse and continuous phases was measured by taking a shear rate sweep from 0.1 to 1000 1/s using a 40 mm cone (angle = 1deg:0min:25 sec) and plate (gap = 29 μm) using a Discovery HR-3 rheometer (TA Instruments, New Castle, USA). All measurements were conducted at 25 °C.

2.4 Interfacial tension measurement

Using a FTA1000 B Class tensiometer (First Ten Angstroms, Portsmouth, USA), the interfacial tension between the disperse and continuous phases was measured by the rising drop method at 25 °C. The surface tension was determined from the shape of the rising drop of the sunflower oil disperse phase before droplet detachment from a hooked needle into the continuous phase. An average of 3 measurements was taken from a pendant disperse phase droplet volume of ~4 μL.

2.5 Continuous Rotary Membrane Emulsification Rig

As shown in Fig. 1a, the rig is made up of four (4) main components: The dispersed phase tank that holds the dispersed phase, an overhead stirrer (Heidolph RZR 2051, Heidolph Instruments, Germany) offering selective rotational speeds from 0 to 2000 rpm, a stainless steel tubular membrane (Microkerf Ltd, Leicester) providing a smooth surface for dispersed phase droplet generation, and a contacting flow cell system that collects the generated droplets and promotes shell gelation. The dispersed phase tank is joined by a connecting tube running from its bottom, via an in-house fabricated lip seal and overhead stirrer, to the membrane. The

membrane is attached to the bottom of the connecting tube using a connector. The bottom of the membrane is covered by a conical shaped stainless-steel bottom cover to prevent the outflow of the dispersed phase and reduce wobble by the rotating membrane during operation. Both the stainless-steel connector and bottom covers have ODs of 14 mm. The connecting tube is held in place by the chuck of the overhead stirrer. Above the overhead stirrer is the in-house fabricated lip seal, made up of leak proof seals and ball bearings. The lip seal decouples the stationary tube/dispersed phase assembly above it from the rotary motion of the tube/membrane assembly beneath it.
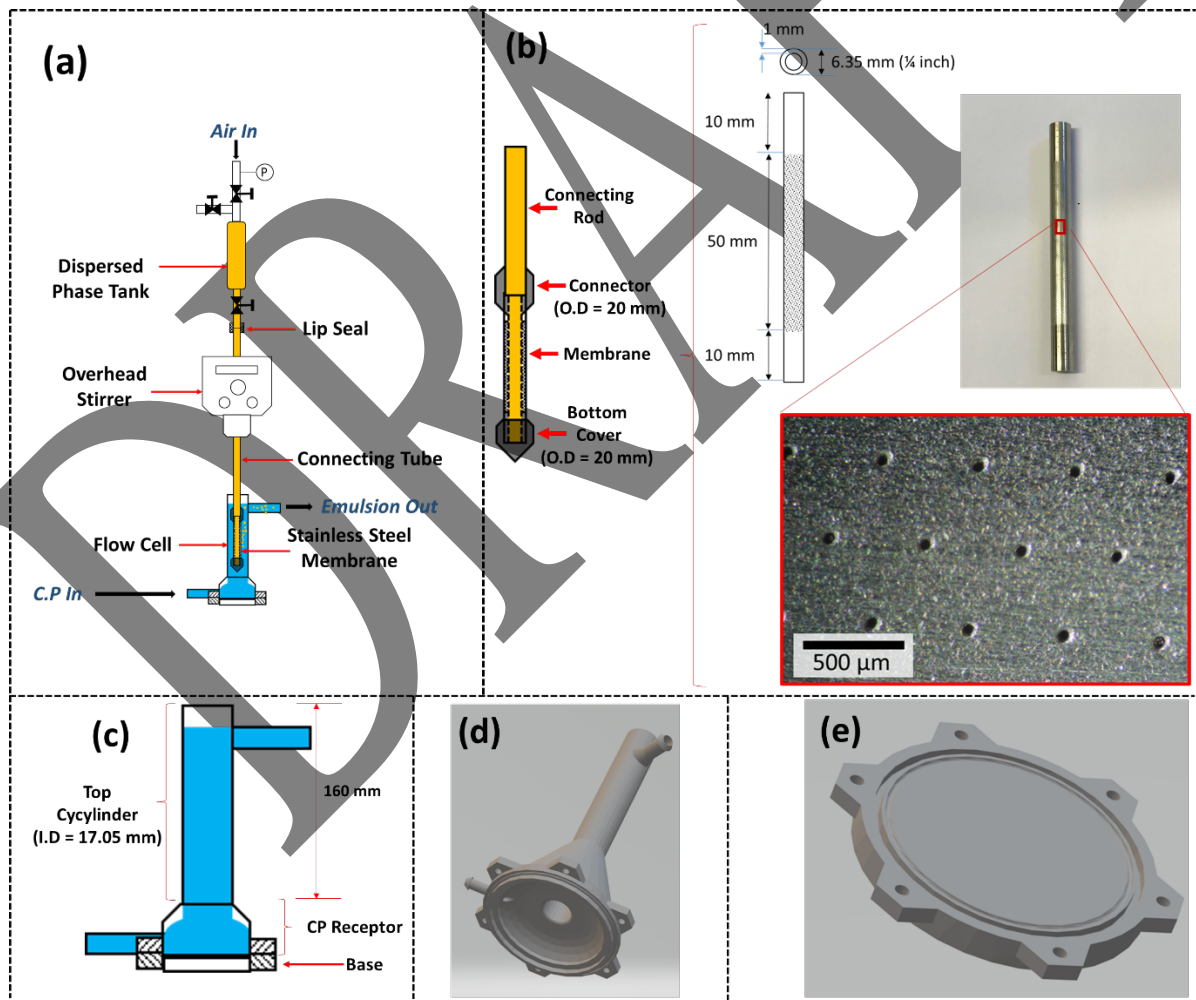
Fig. 1: (a) Continuous rotary membrane emulsification (cRME) rig; (b) stainless steel membrane; (c) flow cell; (d) 3D design of the flow cell's top cylinder and CP receptor; and (e) 3D design of flow cell's base.

As illustrated in Fig. 1b, the membrane has an outer diameter of 6.35 mm and thickness of 1 mm, similar to the dimensions of the tubing to which it is attached. The membrane pore region is located at the middle 50 mm section of its 70 mm length. Owing to the macromolecular stabilizer (keratin), the 30 μm pores were laser drilled to a 500 μm pitch (> 10 times the pore size) to reduce the probability of coalescence occurring during the droplet growth stage before detachment [29].

The contacting flow cell system is made up of a top cylinder (160 mm long with an ID of 17.05 mm), a CP receptor and a bottom cover (Fig. 1c). The cell was 3D printed via Selective Laser Sintering (Shapeways, New York, USA) using a white versatile scratch resistant plastic material (Nylon 12) with a smooth finish in two parts, i.e. the top cylinder/CP receptor (Fig. 1d) and the base (Fig. 1e). The CP receptor has an inlet port to receive the CP. Its inner curved wall eliminates fluid stagnant zones and enhances the steady flow of the CP to the top cylinder where generated emulsions are received and delivered via an outer port. To assemble the cell, an O-ring was placed in the outer groove of the bottom cover while the circular protrusion of the CP receptor was inserted into the inner groove of the base before both parts were screwed to create a liquid tight seal.

2.6 Membrane cleaning and emulsification

Before each test, the membrane was cleaned by immersion in 4 M NaOH, deionized water, 10 wt % citric acid, and finally in deionized water again. For each immersion, a beaker, containing

the membrane and each solution, was placed in an ultrasonic bath for 1 minute, then left to soak for 10 minutes before being transferred to the next solution for sonication. The cleaned stainless-steel membrane was stored in a solution of the CP for use.

For emulsification, tubes were connected to the inlet and outlet ports of the emulsification cell. The cell was initially filled with the CP using a syringe pump (Harvard Apparatus PHD 2000 IV Infusion Pump) until a steady flow of the CP was obtained across the cell. The stainless-steel membrane was then immersed in the cell before appropriate rotational speeds were selected from the overhead stirrer. Care was also taken to ensure that the bottom cell was positioned such that its top cylinder was coaxially symmetrical with the membrane. Upon pressurizing the DP tank with compressed air, just enough to initiate DP flow at 0.1 bar (~2.3 mL/min for all experimental runs), the dispersed phase from the tank passed through the porous membrane radially, and droplets were generated as a result of the wall shear due to membrane rotation. Generated droplets were collected into the cross-flowing continuous phase which streamed out of the cell, by advection, through the outlet port.

2.7 Characterization of generated droplets

A SP400 Metallurgic microscope (Brunel Microscopes) and digital camera (Olympus) was used to visualize and capture optical micrographs of generated droplets. Droplet diameter (i.e volume-weighted mean diameter ($D_{4,3}$)) and uniformity values (an index for a measure of absolute deviation from the median) of the generated droplets were obtained using a Mastersizer 3000 particle size analyzer (Malvern) with a wet dispersion unit operating at 2000 rpm.

2.8 Design of Experiments (DoE)

A Design of Experiments (DoE) was implemented to evaluate the effect of introducing a continuous cross flowing stream to a conventional RME system. Using MODDE Pro 11.0.2 software (MKS Umetrics AB, Sweden), a set of experiments was generated to investigate the effects of 3 selected RME variables as factors on 2 responses functions. Factors investigated were rotational speed (n), OCNF concentration (x_w), and continuous phase flowrate (Q_{CP}), while response functions were droplet diameter and uniformity.

Depending on the operating conditions during membrane rotation, Taylor vortices are generated between the rotating inner and stationary outer cylinder [30, 31]. Though directly proportional to the membrane rotational speed, the shear rate (and resulting shear force) on the surface of the membrane is significantly dependent on the width of the annular gap between the rotating membrane and the stationary cylinder [17]. For the geometry of the system used here, Fig. 2 shows the contour plot of calculated Taylor number values using Eq.s (1) and (2) [32], for continuous phase viscosities (0 - 0.2 Pa.s) and angular velocities (0 - 220 rad s^{-1}):

$$Ta = Re \sqrt{\frac{2(R_2 - R_1)}{(R_1 + R_2)}} \tag{1}$$

$$Re = \omega . R_1 . (R_2 - R_1) . \frac{\rho}{\eta} \tag{2}$$

where Ta is the Taylor number, Re is the Reynolds number, R_1 is the external radius of membrane tube; R_2 is the inner radius of stationary cylinder; ω is the angular velocity; ρ is the density and η is the viscosity of the continuous phase.
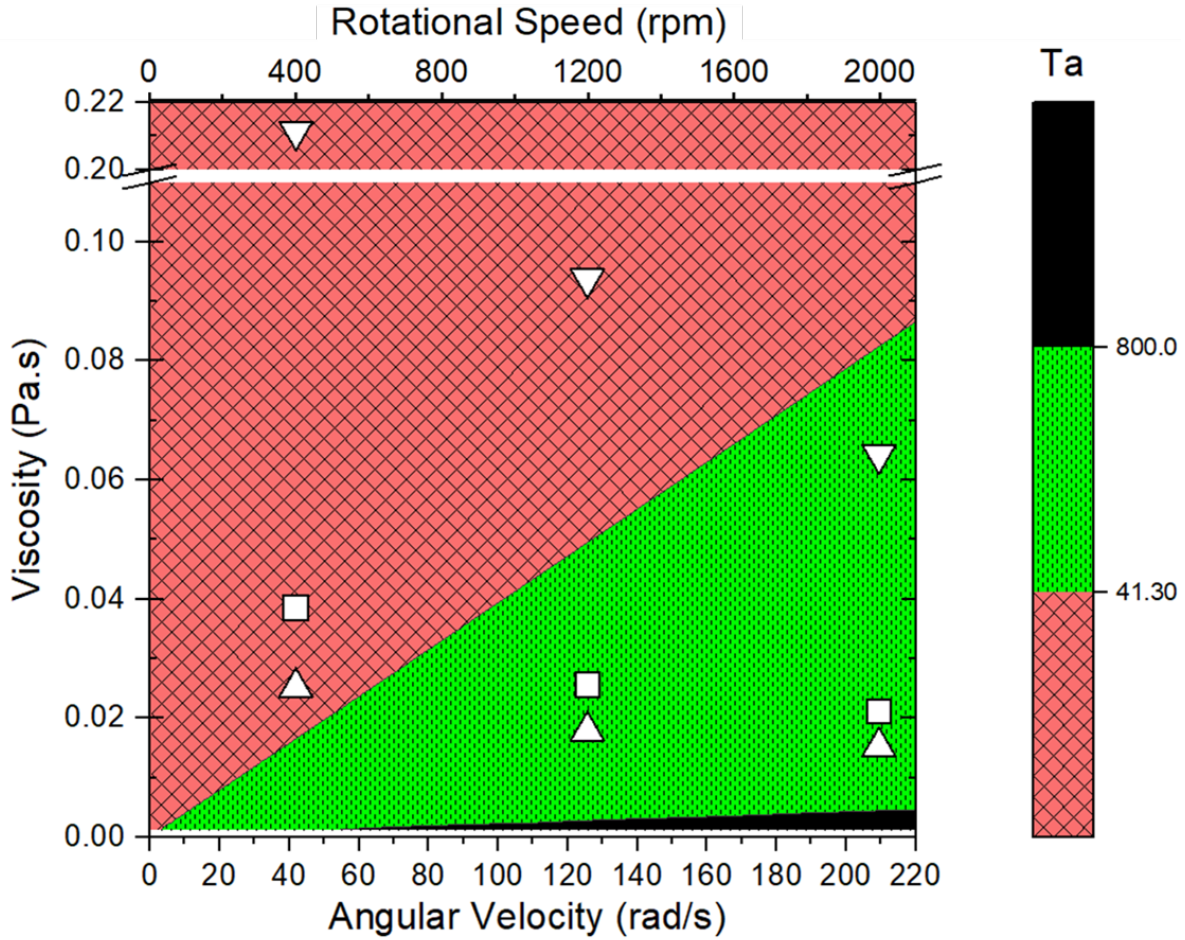
Fig. 2. 2D contour plots showing Taylor number values of the rotary membrane emulsification (RME) component of the combined rig for the chosen continuous phase viscosities and angular velocities used for factor limits and mid-points in the DoE. The continuous phase formulations are: △ 0.50 wt%, ▢ 0.75 wt% and ▽1 wt% OCNF in 1 wt% keratin solution.

Ta values between 41.3 and 800 define the laminar flow within the Taylor vortex regime [19, 32], depicted by the dotted green region. Flow regimes with Ta values below 41.3 are characterized by vortex-free Couette flow which becomes unstable and transitions to form laminar vortices as Ta increases [33]. Above the laminar regime, vortex flow transitions

towards turbulence which can lead to secondary breakage of droplets [32, 33]. The laminar flow regime is ideal for monodisperse droplet generation because the induced laminar vortices aid the movement of generated droplets from the droplet-laden surface of the membrane towards the bulk of the continuous phase and, consequently, reduce the probability of droplet collision, coalescence and non-uniformity [33]. As such, it promotes emulsion stabilization and monodispersity. At constant rotational speed within this regime, the annular gap-dependent shear rate at the membrane surface is constant across the entire surface of the membrane [32].

The design space limits, chosen to be broader than the laminar flow regime, were selected between factor levels of 400 rpm (42 rads^{-1}) and 2,000 rpm (209 rads^{-1}) for rotational speeds (n); OCNF concentrations (x_w) were investigated between 0.5 wt% and 1.0 wt% OCNF in 1.0 wt % keratin solution for their respective low and high factor levels. As a result of the non-Newtonian characteristic of the CP, the viscosity (η) of the OCNF solutions was dependent on both shear rates and concentrations for the chosen factor levels of the DoE investigations (Fig. 2). However, for the range of OCNF concentrations used, there were no significant changes in interfacial tension values between DP and CP (Table S1). Finally, to include the effects of the cross flowing continuous phase, arbitrary low and high factor levels of 5 ml/min and 20 ml/min, respectively, were chosen for the continuous phase flowrate. For the repeat experiments and center point values, the chosen factor limits resulted in a center point at 1200 rpm (rads^{-1}), 0.75 wt% OCNF in 1wt % keratin solution and 12.5 ml/min CP flowrate. Table S2 of the Supporting information summarizes the experimental range and levels of factors.

At the end of each experimental run, the emulsification cell and membrane were cleaned before a new randomized run was carried out. A quadratic model was developed from experimental result analysis to establish a relationship between factors and response functions.

Model fitness and Analysis of Variation (ANOVA) were used to evaluate the developed model. Finally, experimental validation of the model was carried out at an interpolated point within the recommended design space.

3. Results and discussion

3.1 Design of Experiments

The resulting design space, recommended by MODDE, is a Central Composite Face (CCF) design (Fig. S1a). It is composed of a full factorial design (8 vertex points), star points (6 points) placed on the faces of the design space and repeat central points (3 points) that are located at the central core of the design space.

Details of the 17 experimental factor combinations that were subsequently generated with a randomized order of runs are reported in Table S3. Randomization and cleaning of experimental set-up after every experimental run were performed to eliminate biases in the experimental units, and/or annul any influence of systematic factors/independent perturbations that might be difficult to stabilize and control [34].

The magnitudes of the responses for the 17 experimental points are shown in Fig. S1b and Fig. S1c and tabulated in Table S3. Repeat center points had deviations within ± 2.2% for the droplet diameter and ± 3.5% for uniformity. The smallest (N8), largest (N5), most uniform (N13) and most non-uniform (N9) generated droplets are shown in Fig. 3.
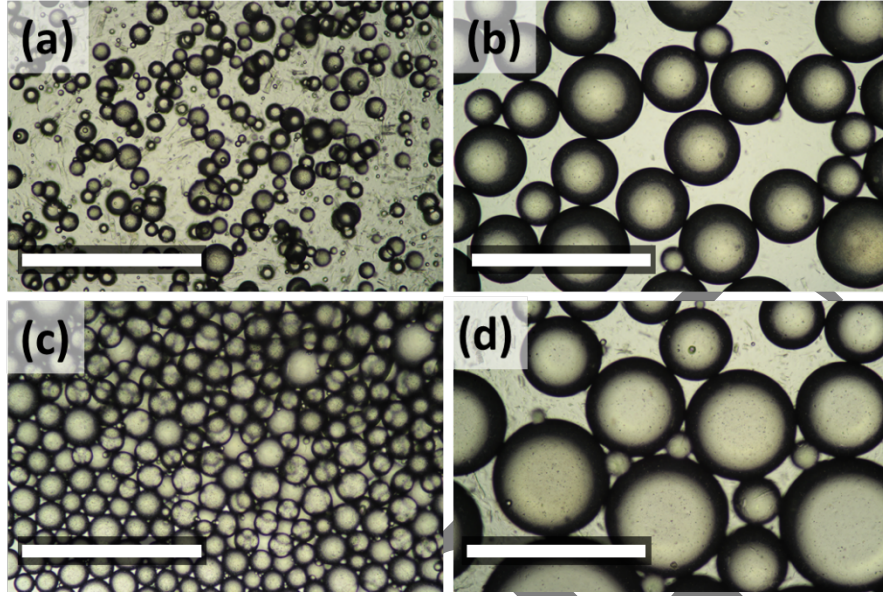
Fig. 3. Optical micrographs of (a) smallest, (b) largest, (c) most uniform and (d) most non-uniform droplets generated from randomized experimental runs. (a) Experiment N8: $n = 2,000$ rpm, 1 wt% OCNF, $Q_{CP} = 20$ ml/min, Droplet diameter = 83.5 μm, and Uniformity = 0.439; (b) Experiment N5: $n = 400$ rpm, 0.5 wt% OCNF, $Q_{CP} = 20$ ml/min, Droplet diameter = 231 μm, and Uniformity = 0.321; (c) Experiment N13: n = 1,200 rpm, 0.75 wt% OCNF, $Q_{CP} = 5$ ml/min, Droplet diameter = 146 μm, and Uniformity = 0.194; (d) Experiment N9: n = 400 rpm, 0.75 wt% OCNF, $Q_{CP} = 12.5$ ml/min, Droplet diameter = 198 μm, and Uniformity = 0.512 Scale bar: (a-c) 1,000 μm, (d) 500 μm .

Using Eq. (3), experimental results were then analyzed and non-linear models developed for each response of size (Y_1) and uniformity (Y_2) to include interactive and square terms as a function of the 3 factors:

$$Y_i = \beta_o + \sum_{i=1}^{3} \beta_i X_i + \sum_{i=1}^{3} \beta_{ii} X_i^2 + \sum_{i<j} \beta_{ij} X_i X_j \qquad (3)$$

where Y_i is the response. β_o is the offset term (intercept constant term) and $\beta_i, \beta_{ii,} \beta_{ij}$ are the linear, square, and interaction regression coefficients, respectively. The model was developed and fitted using a Multiple Linear Regression (MLR) method (Section S3). The summary of fit for both responses is shown in Fig. 4. The parameters, model fit (R^2), prediction precision (Q^2), model validity and reproducibility parameters, were used in determining the fit quality using criteria values of $R^2 > 0.5$, $Q^2 > 0.5$, model validity > 0.25, and reproducibility > 0.5 respectively. See section S3 for further details.
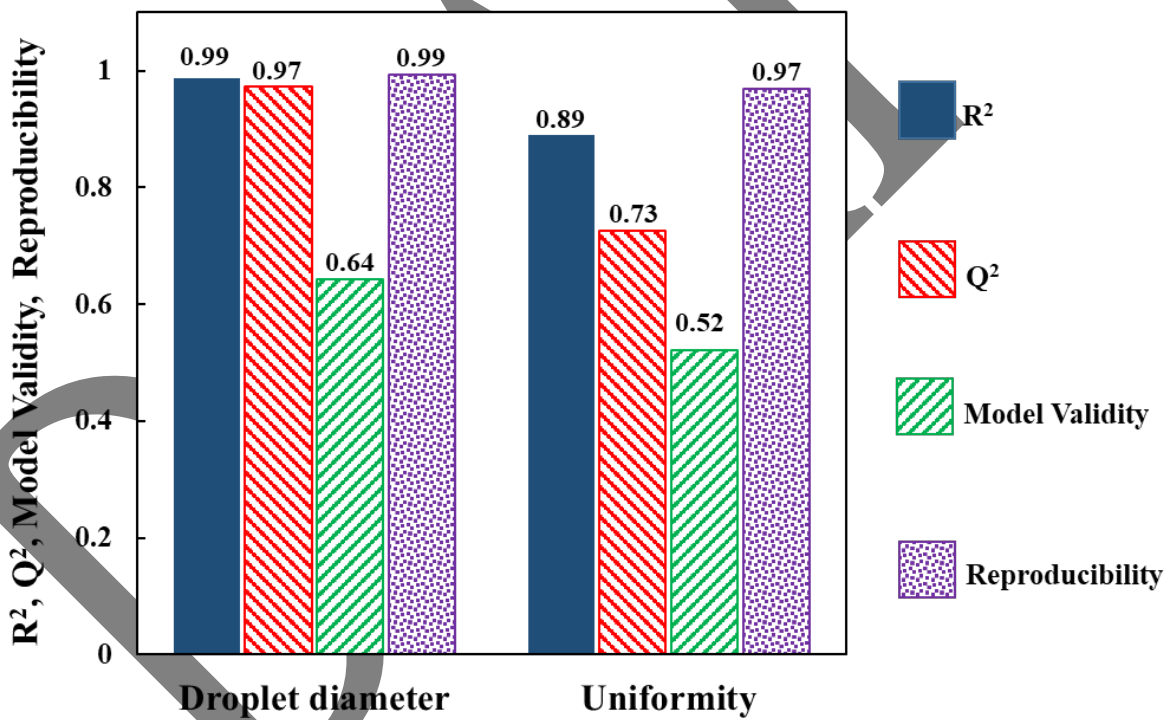

Fig. 4. Summary of fit for transformed responses.

R^2 and Q^2 values for both responses are ≥ 0.89, both above the 0.5 criterion value and within a 0.2-0.3 difference, indicating good model fit (R^2) and (Q^2) predictability. This was due to a good balance of randomization and replicability of experimental runs. Furthermore, the model validity value ≥ 0.52, above the 0.25 criterion value for both responses, indicates the logarithmic transformations applied to both left-skewed untransformed responses (Fig. S2a and S2b) was indeed relevant to obtain a good fit. Such response logarithmic transformations have been necessary to guarantee the normal distribution of responses (ideal in regression analysis) and ascertain that the transformed response values are of the same order of magnitude to improve the accuracy of pure error evaluation and lack of fit tests [35]. The transformed response functions, which are less skewed, are shown in Fig. S2c and S2d. The high reproducibility values, above 0.5, mean that the variation of the center point repeat experiments is less than the overall variation of the response function in both cases (Fig. S3). Following log transformations and variability test of the responses, the least non-significant coefficients of factor interactions and/or squares were then removed from the model. The developed regression model coefficients are summarized in Table S4. The model validity further indicates the absence of outliers from the fitted model, since none of the experimental points deviates from the normal probability line and fit within ±4SD studentized residual values (Fig. S4).

Table S5 shows results of analysis of variation (ANOVA) that was carried out, at a 95% confidence level, on the fitted models using P-value (< 0.05). Results show that lack of fit was non-significant for all models as confirmed by larger values for SD-pe (pure error) × sqrt(F(crit)) than for SD-LoF which were respectively 0.04 and 0.02 for droplet diameter, and 0.09 and 0.05 for uniformity. Also, the model is deemed significant as evident in RSD* sqrt(F(crit)) being smaller than SD-Regression which were respectively 0.02 and 0.21 for

droplet diameter, and 0.08 and 0.2 for uniformity. Hence, for all fit indicators, the summary fit

as evaluated indicates good values for model fit, predictability, validity and reproducibility.

3.1.1 Model Validation

The model was validated experimentally by generating emulsion droplets at an interpolated

point within the design space at 1,300 rpm, 0.6 wt% OCNF and a Q_{CP} of 10 ml/min (Fig. S5).

For statistical validation, this selected interpolated point is neither an experimental nor centre

point. Droplets generated at this point had a diameter of 137 μm and uniformity of 0.22 which

fell within the upper and lower limits predicted by the model (135 μm - 147 μm, and 0.21-0.26

respectively), as detailed in Table S6 of the Supporting information. Optical micrographs of

generated emulsion droplets for validation and size distribution of generated droplets are shown
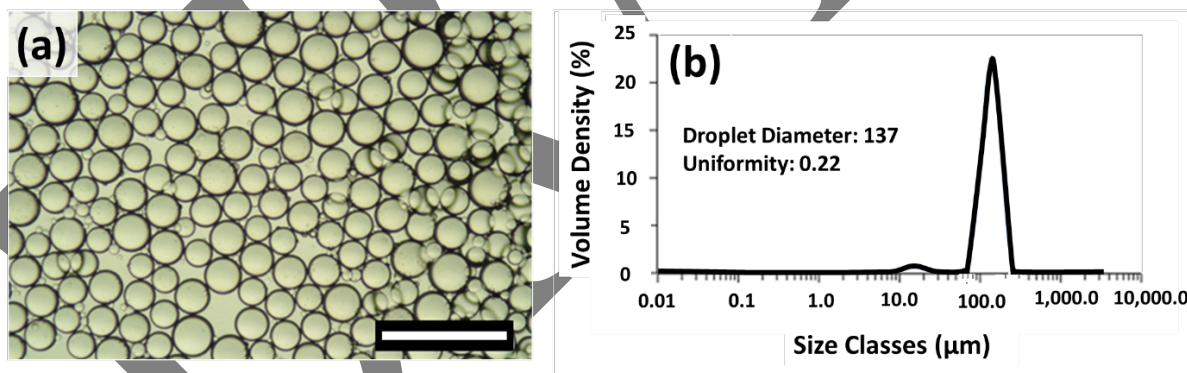
in Fig. 5.

Fig. 5. a) Optical micrograph and (b) Size distribution (volume) of droplets generated at

validation point (1,300 rpm, 0.6 wt% OCNF and a Q_{CP} of 10 ml/min). Scale bar: 500 μm.

3.2 Decoupling continuous phase flow rate (Q_{CP}) from droplet generation

Fig. 6 shows that the effect of Q_{CP} on droplet diameter is insignificant as depicted by the almost horizontal contour lines, across a wide range of rotational speeds (n) and OCNF concentrations (x_w). This is further confirmed in Fig. S1b, where the negligible effect of increasing Q_{CP} can be observed from the four z+ve edges of the design space shown, and in Table S4 with a p value > 0.05. This is a key result, as it demonstrates that the continuous phase flow velocity can be decoupled from shear generation, thereby offering a path to significantly increase the productivity of RME systems. This effect is attributed to the detailed design of the membrane assembly and flow cell (Fig. 1).
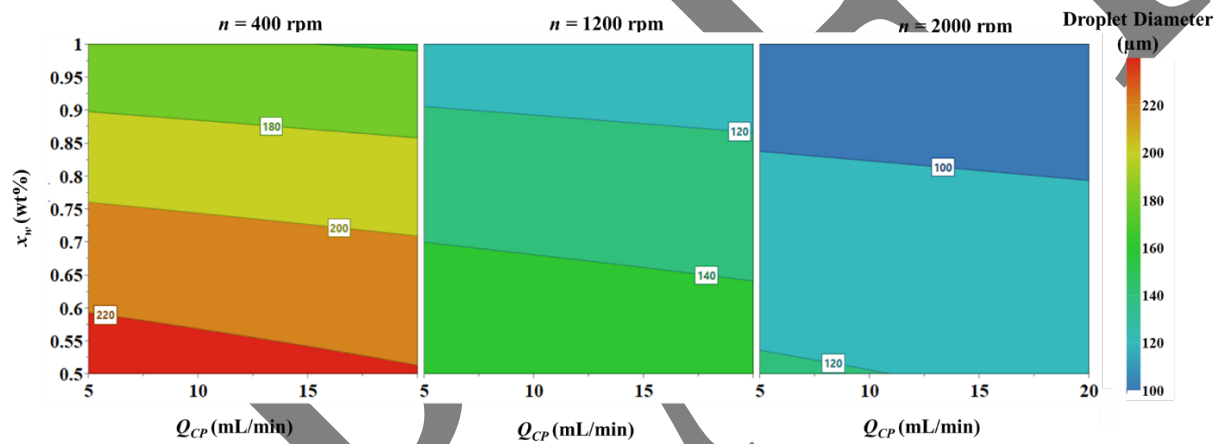

Fig. 6. 4D response contour plot showing the effect of continuous phase flowrate (Q_{CP}) and OCNF concentration (x_w) on droplet diameter at rotational speeds (n) of 400 rpm, 1,200 rpm and 2,000 rpm.

In contrast, there is a significant and antagonistic effect of x_w and n on shear generation and, as a consequence, on droplet diameter (Fig. 7). An increase in x_w results in a reduction in droplet diameter. However, this effect reduces as n increases (left to right), shown by the reduction in the number of contour lines across the images of Figure 6. This reducing influence on droplet

diameter is also depicted in Fig. 7b where, with n increasing from 400 to 2,000 rpm, the reduction rate of droplet diameter (per increase in x_w) decreases by about 55%.
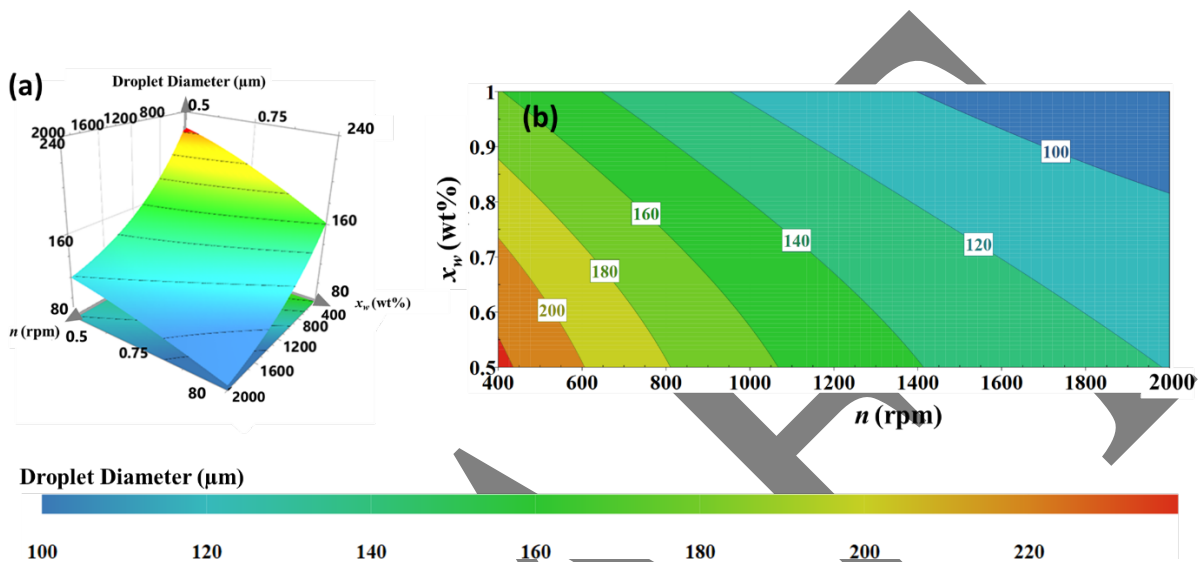

Fig. 7. Effect of OCNF concentration (x_w) and rotational speeds (n) on droplet diameter. (a) Surface plot (b) Contour plot.

In addition to mainly increasing the viscosity of the continuous phase, an increase in OCNF concentration also has a minor effect on reducing interfacial tension between the CP and DP (Table S1) and could act, synergistically, to reduce the diameters of generated droplets. Nevertheless, as quantitatively shown in Table S4, n has a larger antagonistic influence on droplet diameter than x_w and the magnitude X_1 has a lower p value than X_2 for both pure and interactive terms. This is also shown Fig. 7 where, within the design space, the slope for droplet diameter reduction with increasing n is relatively higher than droplet diameter reduction with x_w. The behavior of these wall shear contributing factors (x_w and n) is similar to conventional

batchwise RME systems [17, 18, 32, 36, 37] where increasing shear reduces the droplet diameter with a reducing rate until its influence approximates to a constant droplet diameter.

These results further confirm that not only CP flow has no effect on the shear, but also that CP flow has no interactive effects on n and x_w for droplet diameter variation. Therefore, the CP can be said to have been successfully decoupled from the RME component of the developed rig, and that the wall shear is being governed primarily by membrane rotational shear (i.e viscous shear (x_w) and rotary speed (n) factor dependencies) and not the CP shear.

The continuous phase flowrate (Q_{CP}) has a complex effect on droplet uniformity (Fig. 8) for different values of n and x_w. First, there is a region where the effect on uniformity is negligible across all x_w, as clearly observed in Fig. 8b (i)-(ii). Second, at constant n, an initial increase followed by a reduction in uniformity with increasing Q_{CP} is observed in Fig. 8 across all x_w. The initial uniformity index values increase—which reflects a reduction in generated droplet monodispersity—can be attributed to a disruption of the vortex, caused CP-induced turbulence, formed at constant wall shear magnitudes, that promotes the uniform droplet migration from the surface of the membrane. The corresponding Ta values, which are a function of n and x_w, not Q_{CP}, are reported in Fig. 9.
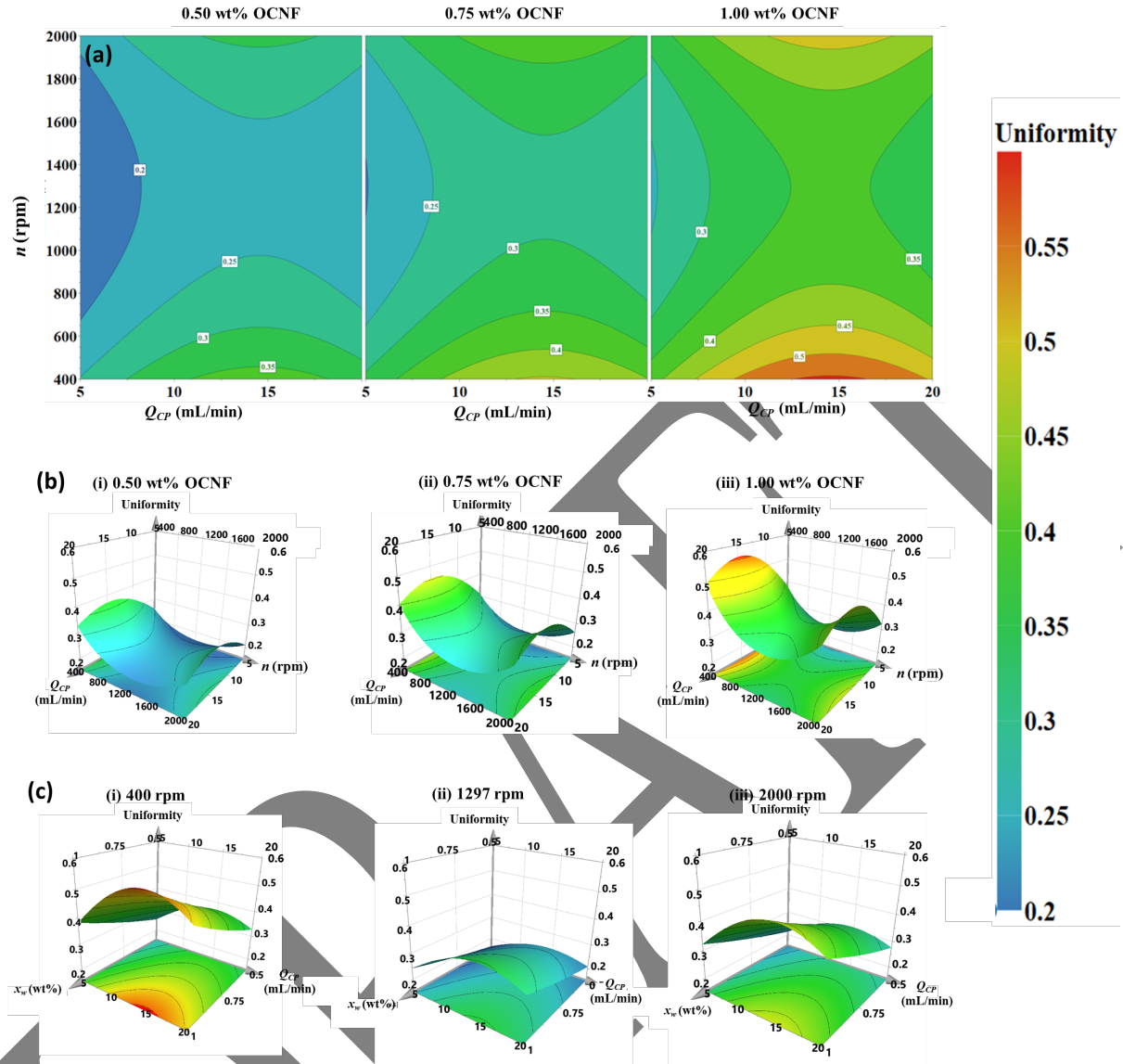
Fig. 8. Effect of experimental variables on droplet uniformity: (a) 4D contour and (b) surface plot showing droplet uniformity variation for different OCNF concentrations (x_w) for (i) 0.50 wt%, (ii) 0.75 wt%, (iii) 1.00 wt% in 1 wt% keratin; (c) surface plot showing droplet uniformity variation at different rotational speeds (n) for (i) 400 rpm, (ii) 1,297 rpm, (iii) 2,000 rpm. The minimum uniformity index value from DoE model is obtained at the optimal rotational speed (n) of 1297 rpm for different OCNF concentrations (x_w).

Increased CP-induced turbulence with an increasing supply of stabilizers from the CP will improve the diffusion of keratin/OCNF to the interface of droplets and, consequently, droplet stabilization. Hence, the subsequent increment in monodispersity is attributed to the droplet stabilization resulting from the combined effect of turbulence and increased supply of stabilizers from the flowing phase i.e. CP. This is not possible in a batch system where generated non-uniform droplets will increase in concentration due to a depleted concentration of stabilisers with continuous CP supply. It is noteworthy that the original uniformity levels at low Q_{CP} cannot be obtained at higher Q_{CP} (Fig. 8a). The effectiveness of vortex-controlled migration for uniformity is, therefore, higher than CP-induced turbulence-controlled uniformity.

3D surface plots in Fig. 8c (i)-(iii) also show a reduction in droplet monodispersity before the occurrence of improved monodispersity for n values of 400, 1,297 and 2,000 rpm. Noticeable is the reduction and flattening of the plot for $n \sim 1,297$ rpm (Fig. 8c (ii)), where the majority of points have higher monodispersity than plots shown in Fig. 8c(i) and 8c(iii). This highlights the optimal n (obtained from the DoE model and noticeable in Fig.8a and Fig.8b) with optimal vorticity formation. This optimal n occurs for all x_w, which can be observed in Fig. 8 a and b.

Hence the combined effect of vorticity induced by rotating the membrane (n) and increased supply of keratin/OCNF (due to the continuously introduced CP flow), improves droplet monodispersity. The balance of this effect on monodispersity is the reason for the existence of the monodispersed regions of Fig. 8a and b which is located around and includes the optimal n region. As a result, the most uniform point within the design space, which was predicted from

the model (as detailed in Section S5), is obtained for $Q_{CP} = 5$ ml/min, $n = 1,297$ rpm and $x_w = 0.5$ wt % OCNF. This point is shown in Fig. S6.

Due to the vorticity and stabilizers' supply balance, enhanced productivity can easily be achieved by simply increasing the DP flux to increase the droplet generation frequency, maintaining n within the optimal region to vary droplet diameter whilst maintain monodisperse droplet generation, and varying the Q_{CP} to obtain targeted emulsion concentrations.

3.3 Understanding vortex formation

For x_w values used within the design space, Fig. 9a shows the droplet diameters (Dd_{DOE}) obtained from the developed DoE and those (Dd_K) obtained from a force balance model [38] as scatter points and line plots, respectively. Diameters from the force model are approximated at zero flux of the DP, with the force balance model based on droplet detachment due to the combined effect of a tangential drag force and the capillary force on a growing droplet from a membrane pore. Hence, Dd_K underestimates the obtained droplets diameters, and Dd_{DoE}/Dd_K is, on average, greater or equal to 1 (Fig. 9b). This ratio tends towards 1 with increasing shear, as the ratio of the angular velocities to the velocity of the disperse phase (the latter being constant in this study) increases.
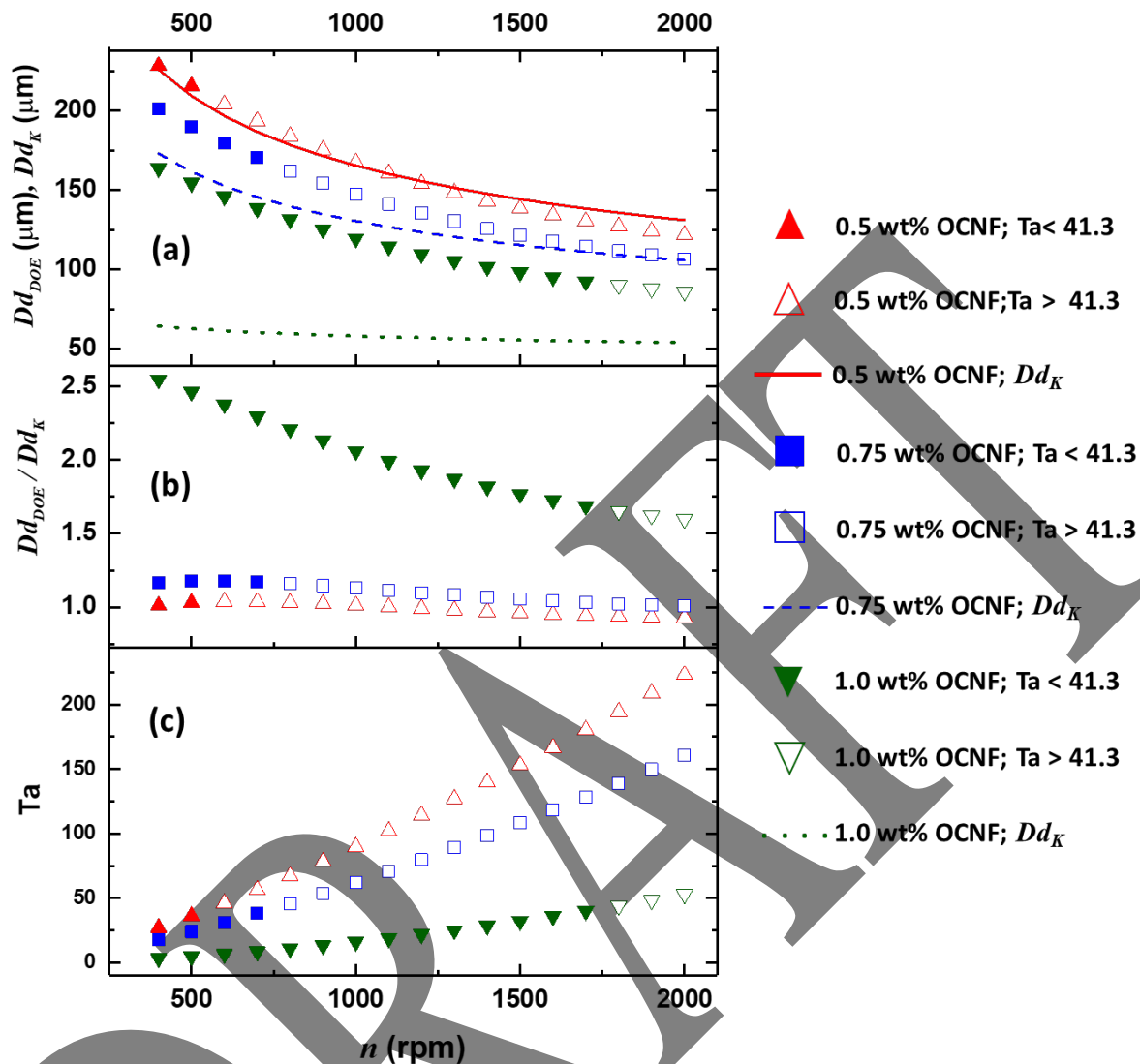
Fig. 9. Generated droplet properties for droplets generated at Q_{CP} = 5 ml/min, x_w = 0.5 wt% ($\blacktriangle$, $\triangle$), 0.75 wt% ($\blacksquare$, $\square$), and 1 wt% OCNF ($\blacktriangledown$, $\triangledown$) across the range of rotational speeds (n) used. Filled symbols show points with Taylor numbers (Ta) below 41.3 (i.e. vortex free) while unfilled symbols indicate otherwise: (a) Generated droplet diameter: Symbols represent droplet diameters estimated from developed DOE model (Dd_{DOE}); lines represent droplet diameters estimated from theoretical force balance model (Dd_K): Solid line shows Dd_K obtained from 0.5 wt% OCNF, dashed line shows Dd_K obtained from 0.75 wt% OCNF, and dotted line shows

Dd_K obtained from 1 wt% OCNF; (b) Dd_{DoE}/Dd_K magnitudes for x_w concentrations; (c) Calculated Taylor numbers.

For x_w = 0.5 and 0.75, below Ta = 41.3 (represented by filled symbols in Figure 9) where laminar flow with Taylor vortex formation is absent, the Dd_{DoE}/Dd_K ratio increases to a peak then begins to reduce at Ta ≥ 41.3 (represented by unfilled symbols in Fig. 9 a-c) where transition to laminar flow with vortex formation occurs [19]. Dd_{DE}/Dd_K is observed to steadily approximate 1, and hence, experimental Dd_{DoE} can be predicted from Dd_K model values. As Ta increases above 41.3, where Taylor vortices form (Fig. 9c), monodispersity initially increases with a steady increase in droplet diameter (Fig. 8). As shear increases further due to increased n, monodispersity reduces for all values of x_w and Q_{CP} (Fig. 8). This uniformity trend is highlighted in Fig. 8 as n increases for all x_w and Q_{CP}. Monodispersity reduction with increasing n is likely due to the presence of satellite droplets formed during droplet pinch off, a common effect in droplets generation systems [39, 40], and observable in Fig. 3a. Such satellite droplets become prominent in narrowing jetting due to high shear rates where droplets form at different points on the jet, with secondary droplet breakage [41], and are non-uniform as a result [42]. Consequently, a slight reduction in Dd_{DoE}/Dd_K ratio is observed in Fig. 9b due to reduction in Dd_{DoE}. Non-uniformity, therefore, in this case is not related to vorticity formation but, rather, is shear induced.

For x_w values of 0.5 wt% and 0.75 wt% in the membrane system geometry used, Fig. 9 shows that transition to Ta = 41.3 occurs at ~553 rpm and ~743 rpm, respectively, but occurs for n = 1,734 rpm (higher than 1,297 rpm) when x_w = 1 wt%. Before laminar vortices form, Couette

flow, which does not promote droplet migration to the bulk of the CP, governs. This implies that for the majority of n values within the design space, laminar vortex formation is absent for $x_w = 1$ wt%. Though droplet detachment still occurs due to shear, the combined effect of the high CP viscosity and absent Taylor vorticities promote poor droplet migration to the bulk of the CP [33]. Hence, droplet coalescence occurs close to the surface of the membrane which leads to droplet diameters being larger than droplet diameters approximated from shear forces (Fig. 9 a and b). However, despite formation of laminar Taylor vortices at $n \geq 1,734$ rpm, uniformity does not improve due to satellite droplet formation and secondary droplet breakage as described earlier. Therefore, during formulation development for cRME systems, to ensure droplet monodispersity during emulsification, the geometry of the membrane system should be designed such that Ta values ≥ 41.3, where laminar vortices occur, can be obtained at a suitable n such that droplet coalescence is curtailed at low n values, and the effect of satellite droplet formation or secondary droplet breakage is minimised at high n values.

3.4 Scale-up potential and comparison with conventional systems

All emulsions in this paper were generated using a DP pressure of 0.1 bar which, combined with the chosen formulation and residence time, resulted in ~12-45 vol% emulsion concentration (depending on the Q_{CP}). For scale-up, increasing the outer diameter (OD) of the membrane, increasing the length of the membrane, and reducing the pitch of the membrane pores can result in increased emulsion concentration. For example, within the design space used here, doubling the OD or length of the membrane would lead to increasing the emulsion concentration by a factor of ~2. Reducing the pore pitch by 50% would lead to an increase by a factor of ~4. A combination of these would result in an emulsion concentration increase by a factor of ~ 16. The design of the 3D printed flow cell can be adjusted to accommodate different

membrane dimensions, with corresponding residence times and Taylor number values which will maintain droplet monodispersity.

The cRME configuration presented here does not suffer from depletion of surfactants or stabilisers which hinders conventional batch RME systems due to the absence of a CP flow (as discussed in Section 3.2). As such, the cRME can be run for extended times with a significantly lower probability of droplet coalescence compared to conventional batch RME system. On the other hand, cross-flow membrane emulsification requires 3 orders of magnitudes higher wall shear to obtain droplets of similar size to those generated with a RME [37]. This implies an emulsion dilution of about 3-4 times that those obtainable with the RME system. Furthermore, increasing the length in cross-flow membrane systems increases the pressure drop across the membrane length, resulting in non-uniform shear distribution across its length, which somewhat limits the scale-up options of such a system. Hence, compared to our system where about ~12-45 vol% emulsion concentration or higher is feasible due to full scale up options, the scalability of the XME is limited and the quality (monodispersity) of generated emulsions will be diminished.

4. Conclusions

A continuous RME rig was designed and fabricated including an easy to clean stainless steel membrane assembly with predefined pore diameters and pitch, and a 3D fabricated flow cell. Using sustainable materials, a detailed study on the effect of introducing a continuously flowing CP to an RME is presented in this work. By varying its flowrate, viscosity and membrane rotational speeds, the extents of the CP influence on generated droplet diameters and

uniformities were detailed using a DoE. Within the design space, emulsion droplets in the 78-241 μm range were generated, with uniformities having a variation index as low as 0.14.

Owing to the tailored geometry and design of the developed cRME system, the flowrate of the continuous phase of keratin/OCNF solution was found to have a negligible effect on the generated sunflower oil droplet diameters but a greater effect on the uniformity. This negligible effect of the continuous phase flow on droplet diameter indicates that the continuous phase flow was successfully decoupled from shear needed for emulsification. Furthermore, for all CP viscosities studied, a range of membrane rotational speed was found to exist where CP flowrate effects were negligible. Hence, the CP flow, while having a minor effect on the magnitude of the wall shear, has a greater effect on vorticity formation between the rotating membrane and the flow cell, which can be controlled. Furthermore, the developed system is predictable, allowing production of emulsions with controlled characteristics with improved productivity.

Continuous operation, the possibility of designing emulsions and increased productivity represent marked advances over conventional cross-flow and rotational membrane emulsification systems, opening the way to a wide range of applications in the food, drug, personal care and agricultural manufacturing.

Declaration of Competing Interest

The authors declare that they have no known competing financial interests or personal relationships that could have appeared to influence the work reported in this paper.

Appendix A

Electronic Supporting information is available and includes DoE analysis and results.

References

[1] T. Nakashima, M. Shimizu, M. Kukizaki, Particle control of emulsion by membrane emulsification and its applications, Advanced Drug Delivery Reviews 45 (2000) 47-56.

[2] M.T. Stillwell, R.G. Holdich, S.R. Kosvintsev, G. Gasparini, I.W. Cumming, Stirred Cell Membrane Emulsification and Factors Influencing Dispersion Drop Size and Uniformity, Ind Eng Chem Res 46 (2007) 965-972.

[3] B.G. Nikolovski, J.D. Bajac, F.L. Martinovic, N. Bogunović, Optimizing stirred cell membrane emulsification process for making a food-grade multiple emulsion, Chemical Papers 72 (2018) 533-542.

[4] N. Aryanti, R.A. Williams, Rotating Membrane Emulsification for Producing Single and Multiple Emulsions, MATEC Web Conf. 156 (2018).

[5] M. Medina-Llamas, D. Mattia, Production of Nanoemulsions Using Anodic Alumina Membranes in a Stirred-Cell Setup, Industrial & Engineering Chemistry Research 56 (2017) 7541-7550.

[6] E. Piacentini, E. Drioli, L. Giorno, Pulsed back-and-forward cross-flow batch membrane emulsification with high productivity to obtain highly uniform and concentrate emulsions, Journal of Membrane Science 453 (2014) 119-125.

[7] R. Holdich, M. Dragosavac, G. Vladisavljević, E. Piacentini, Continuous Membrane Emulsification with Pulsed (Oscillatory) Flow, Industrial and Engineering Chemistry Research 52 (2013) 507-515.

[8] A. Albisa, E. Piacentini, M. Arruebo, V. Sebastian, L. Giorno, Sustainable Production of Drug-Loaded Particles by Membrane Emulsification, ACS Sustainable Chemistry & Engineering 6 (2018) 6663-6674.

[9] J. Coombs Obrien, L. Torrente-Murciano, D. Mattia, J.L. Scott, Continuous Production of Cellulose Microbeads via Membrane Emulsification, ACS Sust Chem Eng 5 (2017) 5931-5939.

[10] E. Piacentini, E. Drioli, L. Giorno, Membrane emulsification technology: Twenty-five years of inventions and research through patent survey, Journal of Membrane Science 468 (2014) 410-422.

[11] R.A. Williams, S.J. Peng, D.A. Wheeler, N.C. Morley, D. Taylor, M. Whalley, D.W. Houldsworth, Controlled Production of Emulsions Using a Crossflow Membrane, Chemical Engineering Research and Design 76 (1998) 902-910.

[12] S.M. Joscelyne, G. Trägårdh, Membrane emulsification — a literature review, Journal of Membrane Science 169 (2000) 107-117.

[13] P.S. Silva, S. Morelli, M.M. Dragosavac, V.M. Starov, R.G. Holdich, Water in oil emulsions from hydrophobized metal membranes and characterization of dynamic interfacial tension in membrane emulsification, Colloids and Surfaces A: Physicochemical and Engineering Aspects (2017) 0-1.

[14] P.S. Silva, M.M. Dragosavac, G.T. Vladisavljević, H.C.H. Bandulasena, R.G. Holdich, M. Stillwell, B. Williams, Azimuthally oscillating membrane emulsification for controlled droplet production, AIChE Journal (2015).

[15] R.G. Holdich, M.M. Dragosavac, G.T. Vladisavljević, E. Piacentini, Continuous membrane emulsification with pulsed (oscillatory) flow, Industrial and Engineering Chemistry Research (2013) 507-515.

[16] R. Holdich, M. Dragosavac, B. Williams, S. Trotter, High throughput membrane emulsification using a single-pass annular flow crossflow membrane, AIChE Journal 66 (2020) 1-10.

[17] G.T. Vladisavljević, R.A. Williams, Manufacture of large uniform droplets using rotating membrane emulsification, Journal of colloid and interface science 299 (2006) 396-402.

[18] N. Aryanti, R.A. Williams, R. Hou, G.T. Vladisavljević, Performance of rotating membrane emulsification for o/w production, Desalination 200 (2006) 572-574.

[19] V. Schadler, E.J. Windhab, Continuous membrane emulsification by using a membrane system with controlled pore distance, Desalination 189 (2006) 130-135.

[20] Q. Li, Y. Wang, Y. Wu, K. He, Y. Li, X. Luo, B. Li, C. Wang, S. Liu, Flexible cellulose nanofibrils as novel pickering stabilizers: The emulsifying property and packing behavior, Food Hydrocolloids 88 (2019) 180-189.

[21] X. Feng, H. Dai, L. Ma, Y. Yu, M. Tang, Y. Li, W. Hu, T. Liu, Y. Zhang, Food-Grade Gelatin Nanoparticles: Preparation, Characterization, and Preliminary Application for Stabilizing Pickering Emulsions, Foods 8 (2019).

[22] S. Zhang, M. Holmes, R. Ettelaie, A. Sarkar, Pea protein microgel particles as Pickering stabilisers of oil-in-water emulsions: Responsiveness to pH and ionic strength, Food Hydrocolloids 102 (2020) 105583.

[23] H. Rajabinejad, A. Patrucco, R. Caringella, A. Montarsolo, M. Zoccola, P.D. Pozzo, Preparation of keratin-based microcapsules for encapsulation of hydrophilic molecules, Ultrasonics Sonochemistry 40 (2018) 527-532.

[24] C.R. Holkar, S.S. Jain, A.J. Jadhav, D.V. Pinjari, Valorization of keratin based waste, Process Safety and Environmental Protection 115 (2018) 85-98.

[25] R.J. Crawford, K.J. Edler, S. Lindhoud, J.L. Scott, G. Unali, Formation of shear thinning gels from partially oxidised cellulose nanofibrils, Green Chemistry 14 (2012) 300-303.

[26] S. Isarankura Na Ayutthaya, S. Tanpichai, J. Wootthikanokkhan, Keratin Extracted from Chicken Feather Waste: Extraction, Preparation, and Structural Characterization of the Keratin and Keratin/Biopolymer Films and Electrospuns, Journal of Polymers and the Environment 23 (2015) 506-516.

[27] V. Calabrese, J.C. Muñoz-García, J. Schmitt, M.A. da Silva, J.L. Scott, J. Angulo, Y.Z. Khimyak, K.J. Edler, Understanding heat driven gelation of anionic cellulose nanofibrils: Combining saturation transfer difference (STD) NMR, small angle X-ray scattering (SAXS) and rheology, Journal of Colloid and Interface Science 535 (2019) 205-213.

[28] V. Calabrese, M.A. da Silva, J. Schmitt, J.C. Munoz-Garcia, V. Gabrielli, J.L. Scott, J. Angulo, Y.Z. Khimyak, K.J. Edler, Surfactant controlled zwitterionic cellulose nanofibril dispersions, Soft Matter 14 (2018) 7793-7800.

[29] N.A. Wagdare, A.T.M. Marcelis, O.B. Ho, R.M. Boom, C.J.M. van Rijn, High throughput vegetable oil-in-water emulsification with a high porosity micro-engineered membrane, Journal of Membrane Science 347 (2010) 1-7.

[30] A.K. Pawlik, I.T. Norton, Encapsulation stability of duplex emulsions prepared with SPG cross-flow membrane, SPG rotating membrane and rotor-stator techniques-A comparison, Journal of Membrane Science 415-416 (2012) 459-468.

[31] T. G.I, VIII. Stability of a viscous liquid contained between two rotating cylinders, Philosophical Transactions of the Royal Society of London. Series A, Containing Papers of a Mathematical or Physical Character 223 (1923) 289-343.

[32] N. Aryanti, R.A. Williams, Analysis of rotating membrane emulsification performance for oil droplet production based on the Taylor vortices approach, Particulate Science and Technology 0 (2017) 1-7.

[33] D.M. Lloyd, I.T. Norton, F. Spyropoulos, Processing effects during rotating membrane emulsification, Journal of Membrane Science 466 (2014) 8-17.

[34] Z.R. Lazic, Design of experiments in chemical engineering: a practical guide, John Wiley & Sons2006.

[35] O. Ly, F. Monchau, S. Rémond, C. Lors, A. Jouanneaux, É. Debarre, D. Damidot, Optimization of the formulation of an original hydrogel-based bone cement using a mixture design, Journal of the Mechanical Behavior of Biomedical Materials 110 (2020).

[36] D.M. Lloyd, I.T. Norton, F. Spyropoulos, Process optimisation of rotating membrane emulsification through the study of surfactant dispersions, Journal of Food Engineering 166 (2015) 316-324.

[37] R.D. Hancocks, F. Spyropoulos, I.T. Norton, The effects of membrane composition and morphology on the rotating membrane emulsification technique for food grade emulsions, Journal of Membrane Science 497 (2016) 29-35.

[38] S.R. Kosvintsev, G. Gasparini, R.G. Holdich, I.W. Cumming, M.T. Stillwell, Liquid–Liquid Membrane Dispersion in a Stirred Cell with and without Controlled Shear, Industrial & Engineering Chemistry Research 44 (2005) 9323-9330.

[39] S.A. Nabavi, S. Gu, G.T. Vladisavljevi, E.E. Ekanem, Dynamics of double emulsion break-up in three phase glass capillary microfluidic devices, Journal of colloid and interface science 450 (2015) 279-287.

[40] E.E. Ekanem, Z. Zhang, G.T. Vladisavljević, Facile Microfluidic Production of Composite Polymer Core-Shell Microcapsules and Crescent-Shaped Microparticles, Journal of Colloid and Interface Science 498 (2017) 387-394.

[41] M. Pathak, Numerical simulation of membrane emulsification: Effect of flow properties in the transition from dripping to jetting, Journal of Membrane Science (2011).

[42] A. Bertrandias, H. Duval, J. Casalinho, M.L. Giorgi, Dripping to jetting transition for cross-flowing liquids, Physics of Fluids 29 (2017).